Behavior of reinforced concrete ring beams strengthened with sustainable materials

Engineering Structures 290 (2023) 116374

Contents lists available at ScienceDirect

Engineering Structures

journal homepage: www.elsevier.com/locate/engstruct

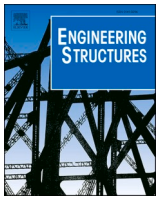

Behavior of reinforced concrete ring beams strengthened with sustainable materials

Ahmed A. Hamoda [a], Boshra A. Eltaly [b], Mohamd Ghalla [a], Qing Quan Liang [c,*]

[a] Civil Engineering Dept., Faculty of Engineering, Kafrelsheikh University, Kafrelsheikh, Egypt
[b] Civil Engineering Dept., Faculty of Engineering, Menofia University, Egypt
[c] College of Sport, Health, and Engineering, Victoria University, PO Box 14428, Melbourne, VIC 8001, Australia

ARTICLE INFO

Keywords:
Ring beams
Engineered cementitious composite
High strength concrete
High strength fiber reinforced concrete
Strengthening techniques
Finite element modeling

ABSTRACT

Reinforced Concrete Ring Beams (RCRBs) have been used in Reinforced Concrete (RC) buildings, tanks, and roof shell structures, such as domes and cones. The curviness feature of RCRBs may result in excessive tensile stresses that may consequently generate critical cracks in concrete, particularly when the beams are constructed with Normal Concrete (NC). This paper presents experimental and numerical investigations on the structural behavior of RCRBs strengthened with sustainable materials. The experimental results on 12 RCRBs constructed with various types of concrete and strengthened with several techniques are presented and discussed. The specimens were made of NC, Engineered Cementitious Composite (ECC), High Strength Concrete (HSC), and High Strength Fiber Reinforced Concrete (HSFRC). Three strengthening techniques were employed for strengthening, including the External Bonded Reinforcement (EBR) with stainless-steel plates (SSPs), the Near Surface Mounted (NSM) with steel bars, and the pre-stressing system. Three-dimensional Finite Element Models (FEMs) were developed by using ABAQUS software to simulate the nonlinear performance of RCRBs. The test results show that the use of sustainable materials in RCRBs can remarkably improve the strength and ductility of RCRBs. In addition, the strengthening techniques are effective in enhancing the responses of RCRBs against the applied loads. Moreover, the thickness and configuration of SSPs significantly affect the ultimate and energy absorption capacities of RCRBs. Finally, a good agreement is observed between numerical predictions and experimental results, suggesting that the finite element model can be employed for further investigations.

1. Introduction

Reinforced Concrete Ring Beams (RCRBs) are not only commonly used in reinforced concrete buildings but also extensively utilized in reinforced concrete water tanks and roof shell structures with revolution forms [1–3]. Such beams are designed to accommodate circular slabs, water tanks, and covering domes or cones to carry the external applied forces. However, the curviness feature of RCRBs leads to the transformation of the applied loads into ring tensile forces. Consequently, the cracking of concrete may occur in initial stages followed by the possible diminishing in yield load and ultimate capacity. Therefore, significant attentions should be paid to those structures made of Normal Concrete (NC) due to its low tensile strength. To overcome this problem, the new generations of fiber reinforced concrete, such as Engineered Cementitious Composite (ECC) and High Strength Fiber Reinforced Concrete (HSFRC), have been used in reinforced concrete structures [4,5]. Aging reinforced concrete structures need to be strengthened and repaired to improve their load-carrying capacity and ductility. Several strengthening techniques have been used by researchers, which include enlarging the concrete cross-section using the flowable High-Performance Concrete (HPC), external/internal bonded fiber-reinforced polymer or steel plates as an additional reinforcement [6,7].

The effectiveness of strengthening techniques for reinforced concrete beams was previously examined [8–13], including the external bonded steel plates and the near surface mounted steel bars. The results showed that these strengthening techniques could significantly improve the strength, stiffness, energy absorption capacity, and ductility of reinforced concrete beams.

The ECC is a class of fiber reinforced cement mortars that exhibits ductile behavior under tensile loading conditions [14,15]. The ECC is characterized by its strain-hardening response rather than the tension-softening phenomenon exhibited by the ordinary fiber-reinforced

* Corresponding author.
E-mail address: Qing.Liang@vu.edu.au (Q.Q. Liang).

https://doi.org/10.1016/j.engstruct.2023.116374
Received 6 November 2022; Received in revised form 29 April 2023; Accepted 23 May 2023
Available online 30 May 2023

cement composites [14,16]. The behavior of ECC ring beams was examined experimentally by Dong et al. [17]. It was found that the ECC ring beams had high load-carrying capacity, ductility, and energy dissipation capacity.

Mariwan and Yousif [18] performed experiments to ascertain the behavior of rectangular reinforced high-strength concrete box-girders under combined torsion-shear-flexure. The results showed that the tested high-strength RC beams had the lower number of cracks. The performance of high-strength fiber reinforced concrete beams strengthened with strips overlay was studied by Banjara and Ramanjaneyulu [19]. It was reported that the use of HSFRC improved the ultimate load and fatigue life of flexural deficient RC beam surpassing that of the control beam. Feo et al. [48] carried out an experimental investigation on freezing and thawing durability of HSFRC. The presence of fibre enhanced the tensile strength in both softening and hardening performance of such concrete elements.

The near surface mounted steel plates/rods were used to strengthen defected reinforced concrete structures by Afefy et al. [20,21]. The steel plates/rods were bonded to the pre-prepared grooves on the concrete cover of the reinforced concrete beam. As steel reinforcement has high tensile strength and ductility, it was used to strengthen RC beams to enhance their shear strengths. The flexural capacity of RC beams was increased by using additional steel bars [22,23].

The effectiveness of ECC and stainless-steel plates (SSPs) in shear strengthening of reinforced concrete beams was evaluated by Hamoda et al. [24]. Experimental findings showed that the strengthening methods can significantly improve the failure pattern and increase the ultimate shear capacity of the studied RC beams by 36%–97% compared to the beam without strengthening. Due to SSPs superior ductility and significant resistance to corrosions, stainless steel has been widely used as a sustainable and durable strengthening material [49]. Such sustainable materials contribute greatly to the performance improvement while maintaining economic value.

The use of SSPs in structural members was examined experimentally and theoretically by Hamoda et al [25] through steel concrete-composite columns. Results showed that the concrete confinement by the stainless-steel tube as well as the vertical stiffeners significantly enhanced the elastic–plastic behavior and ultimate capacity of the columns. The use of stainless-steel in strengthening is considered as a solution to complicated problems particularly when the long-term performance is concerned [26,27].

Large prestressed concrete structures are usually exposed to random cracks and down warping [28]. Zhiheng and Hong [29] examined the distributed displacement estimations of pre-stressed concrete beams by using the experimental method. In the experiment, the neutral axis position, curvature, concrete stress, and vertical displacement were extracted under different load steps. Mansouri et al [30] experimentally studied the flexural strengthening of RC beams using pre-stressing steel bars with the NSM technique. It was shown that the strengthening technique was effective in eliminating the excessive cracking.

Although several studies have been reported on the structural behavior of strengthened RC beams beside strengthening techniques, no experiments have been carried out on RCRBs strengthened with sustainable materials. This paper presents experimental and numerical investigations on the performance of RCRBs made of high-performance concrete and examines the effectiveness of several strengthening techniques incorporating sustainable materials. The main parameters investigated include the concrete type, the strengthening technique, and the embedded length, size and amount of reinforcement required for strengthening. Three-dimensional finite element models developed using ABAQUS are described and verified by experimental measurements. Important conclusions drawn from this study are given.

2. Experimental program

2.1. Specimen details and test program

The current experimental program focused on studying the behavior of strengthened RCRBs subjected to simulated tensile force. Twelve beams with specifications tabulated in Table 1 were tested to failure. The main studied variables were the concrete type, strengthening techniques, and the over lapping length (L_o) and embedded length (L_e) of the reinforcing steel used for strengthening as shown in Table 1. All tested beams were constructed with an identical geometric properties and reinforcement details as shown in Fig. 2. It should be noted that the inner side surface was formed with an inclined position aiming to facilitate the loading process and prevent any movement during testing.

2.2. Material properties and mix proportion

Four concrete mixes were employed in this study that were NC, ECC, HSC, and HSFRC. The mix proportions for each type are given in Table 2. To improve the mechanical characteristics of concrete, two types of fiber reinforced concrete were introduced. One of them was ECC characterized by high strain hardening behavior; while the other one was HSFRC which was made by adding Polyvinyl Alcohol (PVA) fibers to high-strength concrete. PVA fiber with 8 mm length, 1.3 g/cm^3 in density, and 35 μm in diameter was often used [41]. Its Young's modulus was between 30 and 40 GPa and tensile strength was 1000–1600 MPa while its average elongation was about 7%.

The compressive strengths (f_c') of concrete were obtained by testing 150 × 300 mm concrete cylinders and are shown in Table 2. Also, it should be mentioned that the uniaxial tensile test on NC was carried out and the test result was latterly used in numerical study. The tensile test setup, concrete dimensions and perfect failure mode can be seen in Fig. 3. The compressive/tensile stress–strain development is shown in Fig. 4. Fig. 3(a) shows the concrete dimensions and reinforcement detailing of typical test specimen according to US requirements with

Table 1
Test Matrix.

Group	Specimen's ID	Concrete type	Strengthening technique	L_o/L_e	Size of SSPs / bar
G1	B-NC	NC	–	–	–
	B-ECC	ECC	–	–	–
	B-HSC	HSC	–	–	–
	B-HSFRC	HSFRC	–	–	–
G2	B-NC	NC	EBR using SSPs	–	–
	B-NC-SS-0.6	NC		–	0.6 mm
	B-NC-SS-0.8	NC		–	0.8 mm
	B-NC-SS-1.0	NC		–	1.0 mm
G3	B-NC	NC	Post-Tensioning system	–	–
	B-NC-Pr-2D	NC		L_o = 2D	12 mm
	B-NC-Pr-4D	NC		L_o = 4D	12 mm
	B-NC-Pr-6D	NC		L_o = 6D	12 mm
G4	B-NC	NC	NSM using steel bars	–	
	B-NC-S-15D	NC		L_e = 15D	2#10 mm
	B-NC-S-20D	NC		L_e = 20D	2#10 mm

L_o: Over lapping length.
L_e: Embedded length.
SSPs: Stainless Steel Plates.
D: Bar diameter.

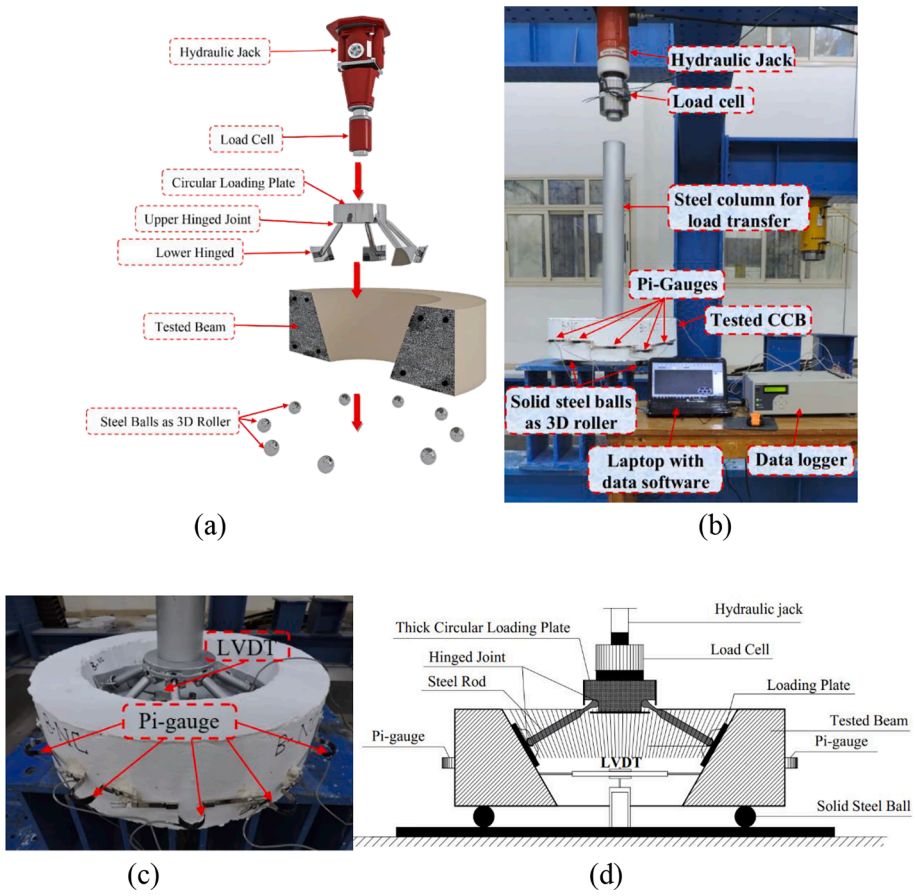

Fig. 1. Test set-up and details of the instrumentations: (a) Schematic of test set-up, (b) Picture of test set-up, (c) Instrumentation, and (d) Schematic details.

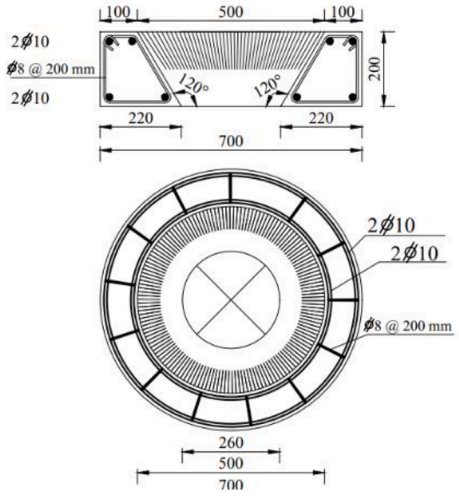

Fig. 2. Geometric and reinforcement details of the beams (Dims; mm).

doubling the dimensions [31].

The mechanical properties of steel elements derived from the uniaxial tensile test. The actual and idealized stress–strain behaviors are shown in Fig. 4(a).

2.3. Description of tested ring beam groups

The ring beam specimens were divided into four groups with respect to the studied parameters as shown in Table 1. The first group was non-strengthened one, included the parameter of concrete type which was introduced to evaluate its impact on the structural behavior of RCRBs. The beams in Group 1 were labeled as B-NC, B-ECC, B-HSC, and B-HSFRC referring to NC, ECC, HSC, and HSFRC, respectively as shown in Table 1.

The second group, the reflection of EBR SSPs and its thicknesses were reported herein through three beams: B-NC-SS-0.6, B-NC-SS-0.8, and B-NC-SS-1.00 with a thickness of 0.60 mm, 0.80 mm, and 1.00 mm, respectively as shown in Fig. 5 (a) and Table 1. Beam B-NC was added and selected as the master one of this group to be compared with.

For the third group, the post-tensioning system was used to strengthen three RCRBs with different L_o as shown in Fig. 5(b). The lengths L_o of beams B-NC-Pr-2D, B-NC-Pr-4D, and B-NC-Pr-6D were 2*D*,

Table 2
Mix proportion and compressive strength of the used concretes.

Concrete	Cement (kg/m^3)	Fine aggregate (kg/m^3)	Coarse aggregate (kg/m^3)	Fly ash (kg/m^3)	Water/binder	PVA Fiber (%) in volume	HRWR (kg/m^3)	f_c' (MPa)	Poisson Ratio
NC	350	700	1150	–	0.43	–	–	25	0.2
ECC	550	440	–	600	0.25	2.00	14.5	44	0.22
HSC	475	655	1050	30	0.32	–	10	56	0.18
HSFRC	450	675	1100	27	0.30	2.00	9.6	72	0.2

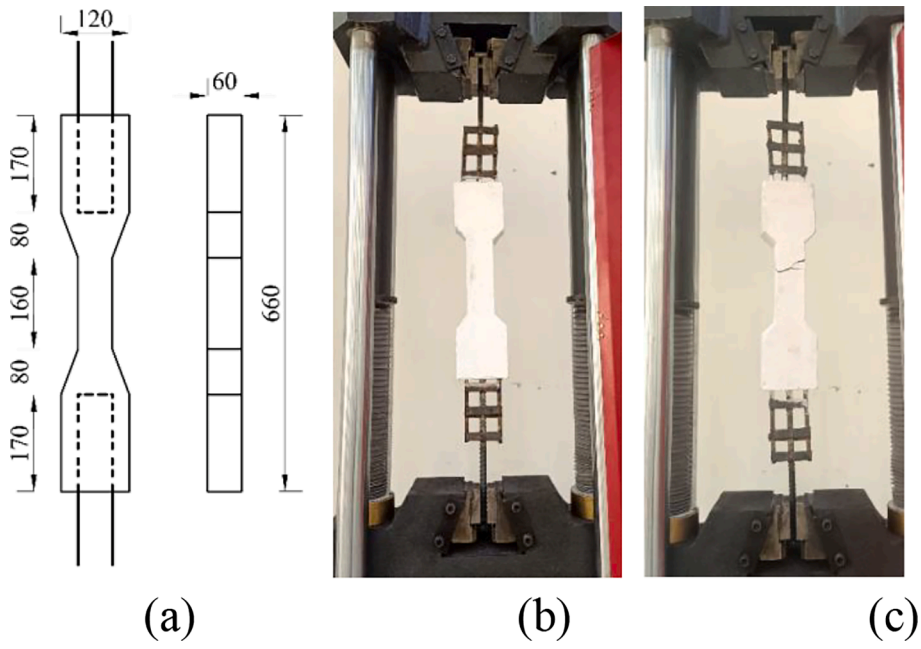

Fig. 3. Uniaxial tensile test for NC: (a) Dimensions, (b) Preparation of test set-up, and (c) Failure for tested sample. (Unit: mm).

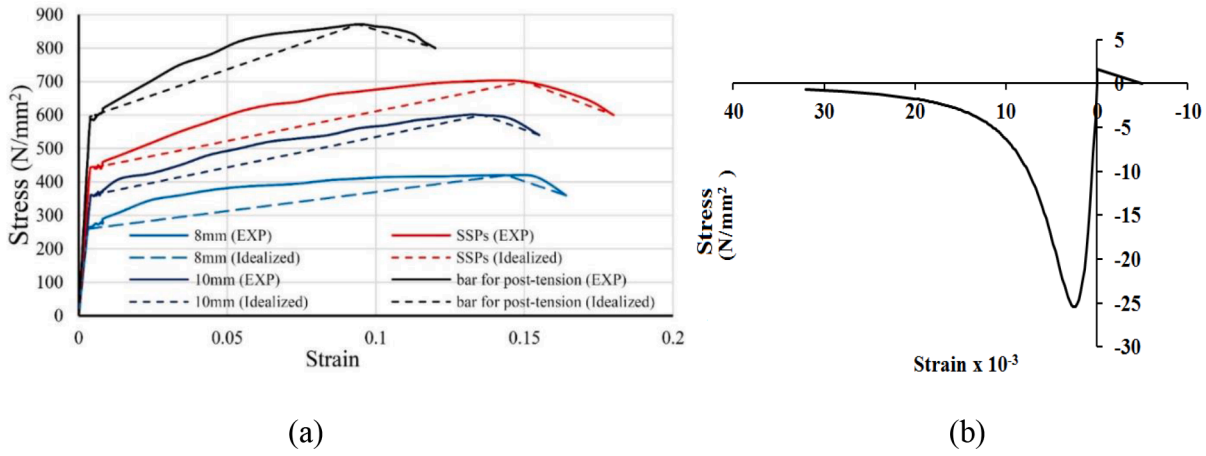

Fig. 4. Stress–strain relationships: (a) Actual and idealized uniaxial stress–strain relationships for steel bars, and (b) Concrete stress–strain law for NC.

4*D* and 6*D*, respectively, where *D* is the bar diameter as shown in Fig. 5 (b) and Table 1. The master beam B-NC was added for comparison purpose.

The last group was used to study the strengthening technique using NSM deformed steel bars with varied L_e. The lengths L_e of beams B-NC-S-15D and B-NC-S-20D were 15*D* and 20*D*, respectively as shown in Fig. 5 (c), while B-NC was the control one as shown Table 1.

2.4. Casting and strengthening preparation

Closed steel formworks were prepared and used for casting all twelve beams shown in Fig. 6. Casting of specimens with NC, ECC, HSC, and HSFRC.

The SSPs employed in Group G2 were implemented experimentally using EBR system as shown in Fig. 7. The outer surface has been roughened as shown in Fig. 7(a). Then, an epoxy adhesive material was used to bond the external SSPs with the concrete surface which was perfectly pre-cleaned as shown in Fig. 7 (b). Such SSPs were placed symmetrically at both top and bottom points of the outer surfaces where third-depth can be existed as shown in Fig. 7(c).

As shown in Fig. 8, the simple post-tensioning system was exploited through screwed steel bars positioned along the outer surface of RCRBs with respect to the schematic diagram shown in Fig. 5(b). Perforated rigid steel fixed end plates, with 20 mm thickness, were previously placed at specified points giving the required overlapping length shown in Fig. 5(b). Screwed steel bars were passed through its hole of the rigid plates. Two bolts were inserted at each bar end which were then scrolled to attend the tension process. The tension force value was recorded using steel strain gauge that was previously mounted on each steel bar as shown in Fig. 8.

The NSM system exploited using embedded steel bars as studied in Group G4 is shown in Fig. 9. Wide grove with 100 mm width was formed in the concrete cover of the outer surface as shown in Fig. 9(a). Using an epoxy adhesive material, as it can be seen in Fig. 9(b), the two ends of the additional deformed steel bars were embedded in concrete core with l_e given in Table 1. Finally, the flowability of ECC was employed for re-covering, forming, and leveling the outer concrete cover as shown in Fig. 9(c).

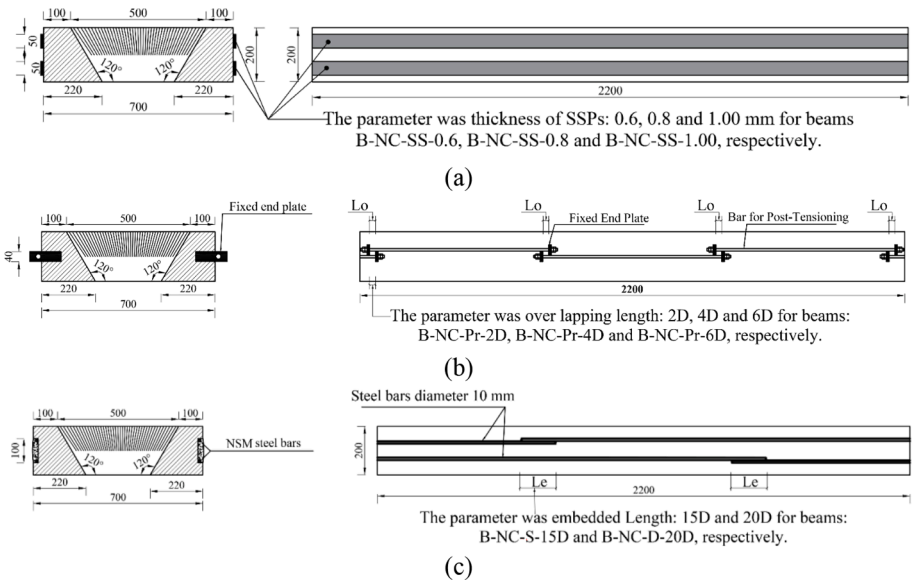

Fig. 5. Geometric details for strengthened groups: (a) Group G2 (strengthening with SSPs), (b) Group G3 (strengthening with pre-stressing system), and (c) Group G4 (strengthening with steel bars). (Dims: mm).

Fig. 6. Formworks and preparation: (a) Steel formworks, and (b) The prepared beams.

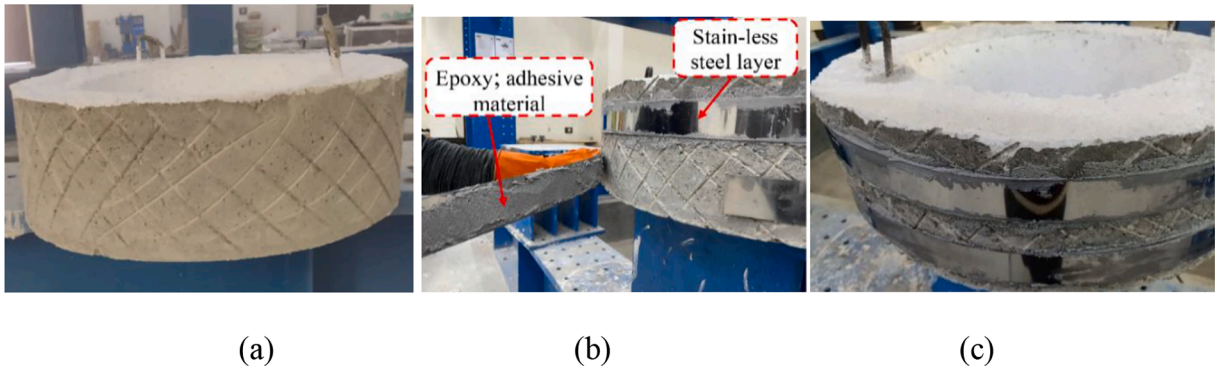

Fig. 7. Strengthening preparation using SSPs for Group G2: (a) Surface adapting, (b) Bonding of SSPs, and (c) Positioning of SSPs.

2.5. Test setup and instrumentation

The loading system was manufactured with an octopus shape producing the simulated horizontal force, as shown in Fig. 1. The octopus system consisted of circular thick loading plate rested over eight rods through hinged joints shown in Fig. 1(c). Such rods were ended with hinged joints over curved rigid loading plates as shown in Fig. 1(d), which were rested directly over the inner inclined surface of the tested RCRB.

The test set-up was constructed to generate a simulated tensile ring force on the tested beam. The beam was rested on movable solid steel balls as roller supports in order to allow the loaded beam for moving at the all-horizontal directions as shown in Fig. 1. During the test operation, the specimen was subjected to a concentric vertical force exerted by a hydraulic jack of 100 ton-capacity attached to a rigid steel frame. A sensitive load cell was used to measure the vertical load as shown in

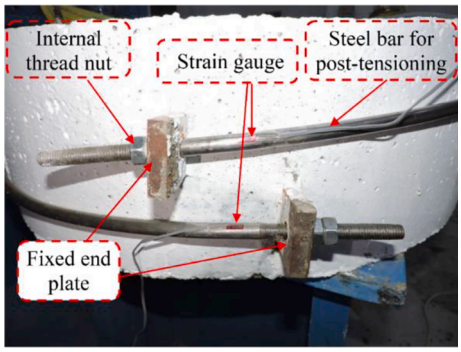

Fig. 8. Strengthening preparation using post-tensioning system for Group G3.

Fig. 1. One Linear Variable Displacement Transducer (LVDT) was attached to the inner diameter of RCRBs to measure the horizontal displacement during the loading process. In addition, eight electrical pi-gauges having 50 mm gauge length were distributed along the outer side of the beam to evaluate and measure the expected vertical cracks. All instrumentations were then connected to Data Acquisition System (DAQ) for recording the readings during the test. The load on each beam was applied incrementally. The development and propagation of cracks were marked up to the failure of the tested beam.

The force control can be introduced by knowing the expected ultimate and failure load that will be resisted by the tested specimen as previously recommended by Belmouden and Lestuzzi [50]. On the other hand, the displacement control can be defined by knowing the expected deformation while the expected load is still unknown as previously executed by Ghahremannejad and Abolmaali [51]. Therefore, the force control was considered in the present study.

3. Test results and discussion

3.1. Crack pattern and failure modes

The cracking patterns of all tested beams can be seen in Figs. 10 to 13. Table 3 summarizes all sensitive results observed experimentally. The main cracking behavior of RCRBs can be observed in Fig. 10(a) in which the collapsed NC beam is shown. The first visible hair crack appeared at the mid-depth of the outer surface at a load value of 55kN (about 33.5% of P_u) as shown in Fig. 10(a). Then, some similar hair cracks appeared at different zones of the outer side of the beam. As the load was increased, such cracks extended and increased upward towards the top surface and downward towards the bottom surface. Beyond that, these cracks started to enlarge encircling the whole cross section passing the inner surface. Just before failure, very few inclined cracks formed at one-third of the depth from either the top or the bottom of the beam as shown in Fig. 10(e). It should be noted that only two inclined cracks shifted horizontally close to the concrete cover where the lap zone of steel bars existed. Finally, the tested beam could not absorb any given load when the sudden concrete crushing occurred close to the two horizontal cracks where the main steel bars were lapped. The ultimate load of the beam was recorded as $P_u = 164$kN. The failure was captured at the lapped bars located at the outer side as a sign of the occurrence of tensile stresses as shown in Fig. 10(f).

Group G1 was basically designed to assess the effect of concrete types on the structural behavior of RCRBs. As mentioned previously, ECC, HSC, and HSFRC were used to construct beams B-ECC, B-HSC, and B-HSFRC, respectively as shown in Table 1. The cracking pattern of this group can be seen in Fig. 10 (b), (c), and (d) for collapsed beams B-ECC, B-HSC, and B-HSFRC, respectively. The appearance of first hair crack was recorded at the mid-depth of the outer surface at a load (P_{cr}) of 57kN, 70kN, and 78kN, respectively as shown in Table 3. The use of HSC

Fig. 9. Strengthening preparation using deformed steel bars for Group G4: (a) Surface adapting (cover removal and cleaning), (b) Installation of steel bars with designed L_e, and (c) Re-covering of concrete surface.

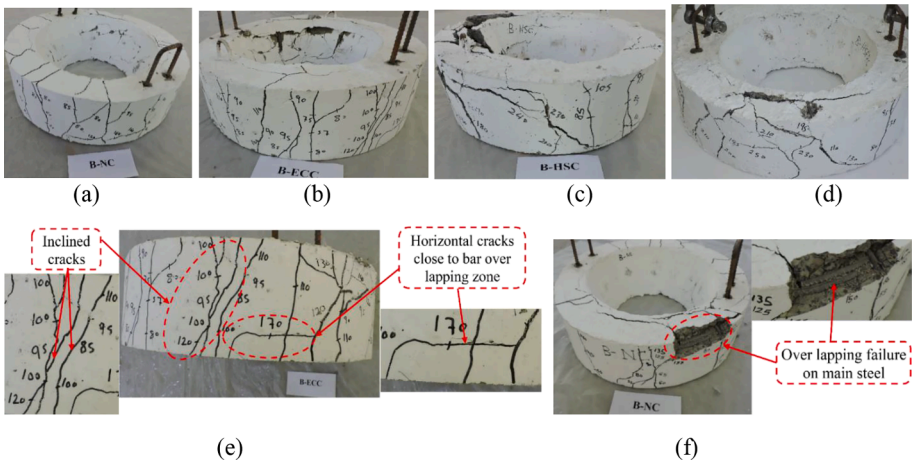

Fig. 10. Crack patterns of Group G1: (a) Master beam B-NC, (b) B-ECC, (c) B-HSC, (d) B-HSFRC, (e) Inclined and horizontal cracks encircling the beam's surface, and (f) Over lapping failure of ring steel bar.

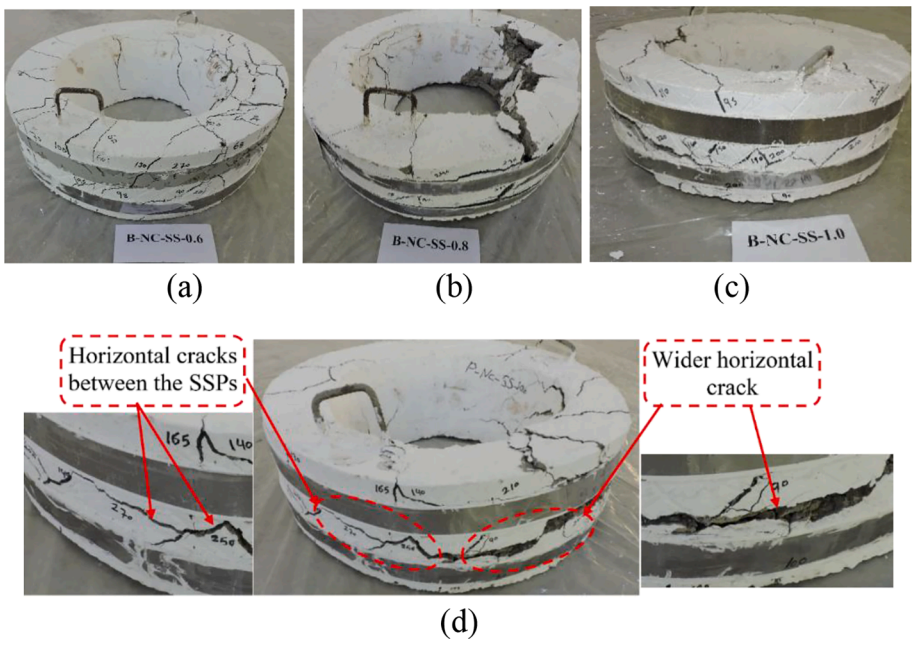

Fig. 11. Crack patterns of Group G2: (a) B-NC-SS-0.6, (b) B-NC-SS-0.8, (c) B-NC-SS-1.00, and (d) Horizontal crack along the outer side surface.

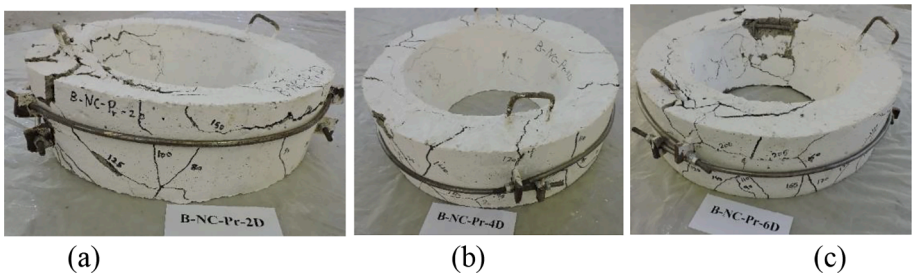

Fig. 12. Crack patterns of Group G3: (a) B-NC-Pr-2D, (b) B-NC-Pr-4D, and (c) B-NC-Pr-6D.

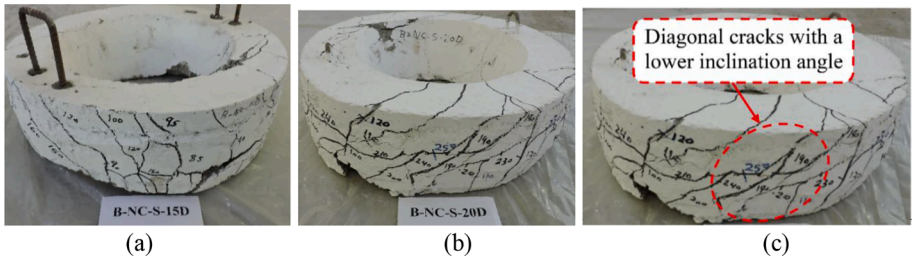

Fig. 13. Crack patterns of Group G4: (a) B-NC-S-15D, (b) B-NC-S-20D, and (c) Diagonal cracks encircling of both side and top surfaces.

and HSFRC increased the cracking load (P_{cr}) by about 27% and 41%, respectively when compared to NC.

Then parallel vertical cracks, with different widths, occurred at different zones of the outer side as shown in Fig. 10. At each load increment, these vertical cracks increased and enlarged upward and downward towards both top and bottom surfaces, respectively. However, the ECC beam presented approximately higher number of cracks with small widths compared to the HSFRC beam. Moreover, the HSFRC beam showed higher number of smaller cracks than those of HSC or NC beams as shown in Fig. 10(c). Similar to the master beam, the cracks appeared at the outer surface and started to encircle the whole cross section passing the four side surfaces. Beyond that and with higher load values, some inclined cracks in conjunction with or without the depiction of few horizontal cracks occurred at the outer surface as shown in Fig. 10(e). Failure occurred close to the zone where horizontal or inclined cracks were formed. Fig. 10(f) shows that the failure was detected at the over lapping zone of steel bars because of excessive tensile stresses. The achieved ultimate loads (P_u) of B-ECC, B-HSC, and B-HSFRC beams were 180 kN, 254 kN, and 254 kN, respectively, as given in Table 3. Table 3 illustrates that the application of HSC contributed to the ultimate load by about 54%. Also, the ECC enhanced the cracking behavior, especially the numbers and widths of cracks. The application of HPCs in such kind of beams enhanced the total structural performance. This was appeared clearly in the final failure mode, where the collapse became more plastic with giving a greater number of cracks, which is desirable in the collapse of the concrete elements.

Group G2 was exploited to evaluate the EBR strengthening technique incorporating SSPs through three tested beams: B-NC-SS-0.60, B-NC-SS-

Table 3
Test Results.

Group	Specimen ID	Cracking Stage				Ultimate Stage			Elastic Stiffness Index (K)	K_B/K_0	Absorbed Energy (E)	Failure Mode
		P_{cr} (kN)	P_{crB}/P_{crB0}	Δ_{cr} (mm)	W_{cr} (mm)	P_u (kN)	P_{uB}/P_{uB0}	Δ_u (mm)				
G1	B-NC	55	1.00	1.18	0.21	164	1.00	4.81	46.61	1.00	249.14	O
	B-ECC	57	1.03	0.22	0.05	180	1.09	2.62	259.09	5.55	611.90	O
	B-HSC	70	1.27	0.27	0.2	254	1.54	2.01	259.25	5.56	287.49	O
	B-HSFRC	78	1.41	0.32	0.15	258	1.57	2.98	243.75	5.22	344.67	O
G2	B-NC	55	1.00	1.18	0.21	164	1.00	4.81	46.61	1.00	249.14	O
	B-NC-SS-0.6	60	1.09	0.85	0.18	279	1.70	4.9	70.58	1.51	414.92	S
	B-NC-SS-0.8	70	1.27	0.71	0.17	284	1.73	4.28	98.59	2.11	440.42	S
	B-NC-SS-1.0	70	1.27	0.46	0.17	283	1.72	3.78	152.10	3.26	493.80	S
G3	B-NC	55	1.00	1.18	0.21	164	1.00	4.81	46.61	1.00	249.14	O
	B-NC-Pr-2D	60	1.09	0.27	0.14	158	0.963	2.53	220.2	4.72	178.70	C
	B-NC-Pr-4D	75	1.36	0.30	0.14	190	1.158	1.81	250.0	5.36	176.30	C,O
	B-NC-Pr-6D	85	1.54	0.32	0.12	211	1.28	2.04	265.62	5.69	194.25	C,O
G4	B-NC	55	1.00	1.18	0.21	164	1.00	4.81	46.61	1.00	249.14	O
	B-NC-S-15D	75	1.36	0.56	0.14	200	1.21	2.30	133.92	2.87	246.17	B
	B-NC-S-20D	100	1.81	0.70	0.15	261	1.59	2.85	142.85	3.06	252.20	B

O: Over lapping failure.
S: Splitting failure.
C: Concrete crushing between two fixed end plates failure.
B: Bar pulling-out.

0.80, and B-NC-SS-1.00. The crack pattern of this group can be seen in Fig. 11. The appearance of first crack was recorded at load value ranged from 60 kN to 70 kN (about 21.5% and 24.7% of P_u) as remarked in Fig. 11. After the occurrence of some similar cracks, inclined cracks started to appear at region in between the two SSPs as shown in Fig. 11 (d). These cracks were marked at loads within range of about 53% to 57% of P_u. Just before failure, some horizontal cracks appeared at the interface zone between the SSPs and beam surface, which may be caused by the interface debonding. Finally, all specimens failed due to the sudden wider horizontal cracks, shown in Fig. 11 (d). The recorded ultimate loads (P_u) were 279 kN, 284 kN, and 283 kN for beams B-NC-SS-0.60, B-NC-SS-0.80, and B-NC-SS-1.00, respectively. It is noted that the cracks in concrete developed gradually with increasing the applied load. Three stages were identified. The first stage was the vertical cracks representing the initiation of ring tensile forces. The second stage was the inclined cracks referring to the beginning of stainless-steel resistance. Finally, the load resistance was ended by the occurrence of horizontal splitting cracks because of bonding failure.

Group G3 was designed to study the pre-stressing technique at the outer surface of RCRBs. Fig. 12 shows the crack pattern of all tested beams in Group G3. The first crack formed at the mid-depth of the outer surface at the load (P_{cr}) values of 60 kN, 75 kN, and 85 kN for beams B-NC-Pr-2D, B-NC-Pr-4D, and B-NC-Pr-6D, respectively. Then, under higher loads, all beams presented remarkable diagonal cracks attempting to encircling the outer surface as manifested in Fig. 12. This may refer to beginning of the desired contribution generated by prestressing system. Then as the load was increased, one horizontal major crack appeared in the top zone of the beam. Before the beam failed, some cracks with larger widths formed at only one zone close to the first major one. Beam with lower L_o (i.e. L_o = 24 mm, B-NC-Pr-2D) had concrete crushing between the two fixed end plates in conjunction with the sudden concrete crushing close to the horizontal major crack. The other two beams B-NC-Pr-4D and B-NC-Pr-6D showed the overlapping failure of the top bars followed by concrete crushing. The ultimate loads (P_u) of the beams B-NC-Pr-2D, B-NC-Pr-4D, and B-NC-Pr-6D were measured as 158 kN, 190 kN, and 211 kN, respectively.

The main purpose of Group G4 was to examine the effectiveness of the NSM strengthening technique for RCRBs including. Table 3 illustrates that strengthening decelerated the appearance of first crack in up to the load values of 75 kN and 100 kN, respectively. The cracking loads of B-NC-S-15D and B-NC-S-20D increased by 36% and 81% compared to that of the beam B-NC. The first visible hair crack formed at the zone in between the two additional bars as shown in Fig. 13 (c). Then, few cracks grew from the first one at a load ranging from 52% to 65% of P_u.

As the load was increased, some inclined diagonal cracks started to form as shown in Fig. 13 (c). Such cracks continued to enlarge and propagate upward towards the top surface and downward towards the bottom surface encircling the beam's cross section. Moreover, it was observed that the horizontal cracks extended from inclined ones occurred at the loads of 180 kN and 240 kN for beams B-NC-S-15D and B-NC-S-20D, respectively. Finally, the beams B-NC-S-15D and B-NC-S-20D could not sustain any applied loads. The ultimate loads of B-NC-S-15D and B-NC-S-20D were 200 kN and 261 kN, respectively, which were improved by about 21.9% and 59%, respectively, compared to the master one made of NC.

3.2. Ultimate loads

Table 3 compares the ultimate load values of all tested beams. The use of high strength concrete such as HSC or HSFRC resulted in an increase in the ultimate capacity by about 54% and 57%, respectively. The higher enhancement was awarded to the group used SSPs (G2). In this context, Table 3 indicates that utilizing EBR with SSPs as the strengthening technique increases the ultimate load by 70%-73%. It should be noted that the thickness of SSPs appeared to have a similar effect on the ultimate capacity.

For beams in Group G4 in which NSM was used with additional steel bars, the ultimate load increased with an increase in L_e. The ultimate loads of beams with L_e values of 15D and 20D increase by about 21% and 59%, respectively. It was observed that, although all strengthening techniques enhanced the ultimate capacity, the applications of SSP with thickness not less than of 0.6 mm was qualified to present the higher augmentation.

3.3. Absorbed energy

Table 3 presents the values of absorbed energy (E) calculated for the tested beams as the integration of the area under the load–displacement curve. It was found that the new generation of HPCs resulted in a better improvement in the energy absorption capacity. In this context, Table 3 illustrates that E values observed from RCRBs made of ECC and HSFRC (specimens: B-ECC and B-HSFRC) are 145% and 38% higher than those estimated from NC beam (B-NC), respectively. Due to its higher strain hardening performance, the higher contribution for the absorbed energy

is credited to the ECC as shown in Fig. 14.

Experimented results show that there is an essential contribution of SSPs to the performance of the structure. This may be evidenced by not only the increase in the ultimate load but also the enhancement recorded in E value which is 60%-70% higher than that of non-strengthened beam.

3.4. Load displacement response and elastic index

The measured load-horizontal displacement curves of tested beams are depicted in Fig. 15. Table 3 shows the horizontal displacement values corresponding to the cracking and ultimate stages (Δ_{cr}) and (Δ_{cr}), respectively. As an impression of the linear exhibition, the elastic stiffness index (K) estimated as the slope of the linear curve is provided in Table 3.

Generally, the presence of HPCs enhanced the load–displacement behavior compared to that made of NC shown in Fig. 15(a). Moreover, this can be confirmed by the estimated K-value since all beams made of HPCs enhanced the K-values which were 5.2 to 5.5 times higher than that of NC beam (master one) as shown in Table 3. However, negligible difference at linear stage was observed when comparing the all types of HPCs (ECC, HSC, HSFRC) with each other's as shown in Table 3 and Fig. 15(a).

Fig. 15(b) indicates that the load–displacement behavior of RCRBs was enhanced by increasing the thickness of SSPs. Moreover, the existence of SS plates resulted in a better contribution to the elastic behavior as manifested in K-value shown in Table 3.

Beams strengthened with prestressing technique improved the K-values compared to that obtained by master beam. At initial stage, the displacement developed by beam having L_o equaled to 2D was smaller than that recorded by other counterparts as shown in Fig. 15(c). This enhancement was estimated by about 4.7–5.7 times over than that recorded by the master beam as shown in Table 4. In similar context, and as it was expected to be, the larger distance between two interacted fixed end plates (L_o as shown in Fig. 15(c)) resulted in an obvious enhancement in both cracking and ultimate stages.

The use of additional steel bars, as experimented in G4 led to an increase in the ultimate capacity with lower displacement as depicted in Fig. 15(d). Beams B-NC-S-15D and B-NC-S-20D exhibited a similar behavior from earlier loading up to failure. However, it is worth noting that the technique of NSM with embedded steel bars improved the elastic stiffness 2.8 to 3.0 times that of the non-strengthened beam B-NC.

4. Numerical simulation

4.1. Constitutive modeling of materials and sensitivity of numerical parameters

The Concrete Damage Plasticity (CDP) model has been qualified for modeling the plastic mechanical performance of concrete because of its capability of simulating damage arising from cracking and nonlinear deformation in tension and compression [32–35]. Plastic damage models for concrete are available in ABAQUS [36] with evaluation of yield surface hardening variables and are frequently used for conventional concrete proposed by Lubliner et al. [37]. Both splitting tension beside compressive strength tests carried out experimentally were used for adopting concrete material stress–strain relationship utilized for modeling. Compression stress–strain law was developed with respect to the formula proposed by Carreira and Chu [38]. Besides, uniaxial tensile stress–strain behavior was introduced as a linear behavior up to ultimate level based on the splitting tensile test reported previously [25,39]. Material constitutive model of NC subjected to compressive and tensile stresses can be seen in Fig. 4.

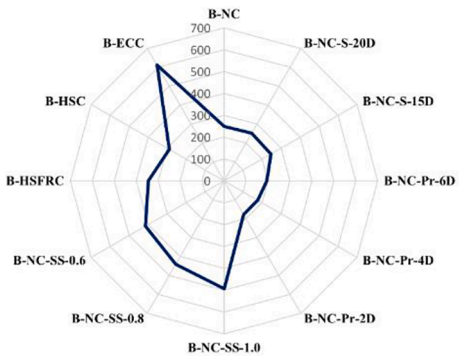

Fig. 14. The absorbed energy (E) for all beams (kN.mm).

Several trials were executed in order to capture the better constitutive parameters required to describe CDP model used to define the NC. Such parameters were the eccentricity (e), dilation angle (ψ), viscosity relaxation parameter (μ), ratio of biaxial to uniaxial compressive yield stresses (f_{bo}/f_{co}), and ratio of the second stress invariant on the tensile to compressive meridian (K_c). The K_c value is between 0.64 and 0.80 as previously recommended [37,40–45]; an acceptable data was impressed with the default value of 0.66 reported by ABAQUS [33]. The ratio of f_{bo}/f_{co} is between 1.10 and 1.16 based on previous studies [45,46]; however, the value of 1.16 was adopted in the present study. The defaulted e value was 0.1. Several trials were undertaken with various relaxation parameters varied from 0.00 to $0.5 * 10^{-8}$, $1.0 * 10^{-8}$, $1.5 * 10^{-8}$, $1 * 10^{-7}$, $1.5 * 10^{-7}$, $1 * 10^{-6}$, $1 * 10^{-5}$, $1 * 10^{-4}$, and 0.001. However, as reported previously [33], the zero-value presented sensible results compared to the very stiff model with higher viscosity as previously mentioned [25,47]. Based on several trials with different dilation angles (varied from 10° to 55°) better outcomes were provided herein with the default value of 35°.

Two different steel bars were used in this numerical modeling: 8 mm and 10 mm diameter steel bars with the same material properties specified earlier in Fig. 4. The uniaxial stress–strain relationships obtained experimentally are illustrated in Fig. 4. In order to gain a better numerical model with less computational cost, the actual stress–strain relationship determined experimentally was idealized to piecewise linear one as idealized in Fig. 4. An elastic zone was considered prior to yield stage followed by the hardening and softening performances with respect to ultimate and failure levels, respectively.

4.2. Model set-up

A nonlinear three-dimensional Finite Element Model (FEM) was constructed to simulate the responses of tested RCRBs in Group G2 that were loaded statically up to collapse. The commercial software ABAQUS was utilized to develop the FEM. A detailed description of the model in terms of geometry, element types, boundary conditions, and interactions is given herein.

The continuum, three-dimensional and eight-node linear hexahedral solid element with reduced integration (C3D8R) in ABAQUS was used to model the concrete and thick steel plates. The reinforcement steel bars were defined using the two-node and linear truss elements (T3D2). Four-node shell element with reduced integration (S4R) was employed to simulate the SSPs. All elements were assembled to form the whole model. An overview of the mesh and a schematic representation of the various modeling assumptions are shown in Fig. 16(a). Taking into consideration the trapezoidal shape of cross section, the whole model has been meshed with respecting to dividing the outer edges of the ring beam. The number of executed elements, considering the less computational cost with better outcomes, were as follows: 384 elements, 24 elements, 32 elements, and 84 elements, respectively, for concrete part, stainless steel strips, circular steel bars and stirrups.

Thick steel plates with higher stiffness were introduced in imitation of the loading plates over the inner inclined side as highlighted in Fig. 16. Like the boundary conditions mentioned in the experimental

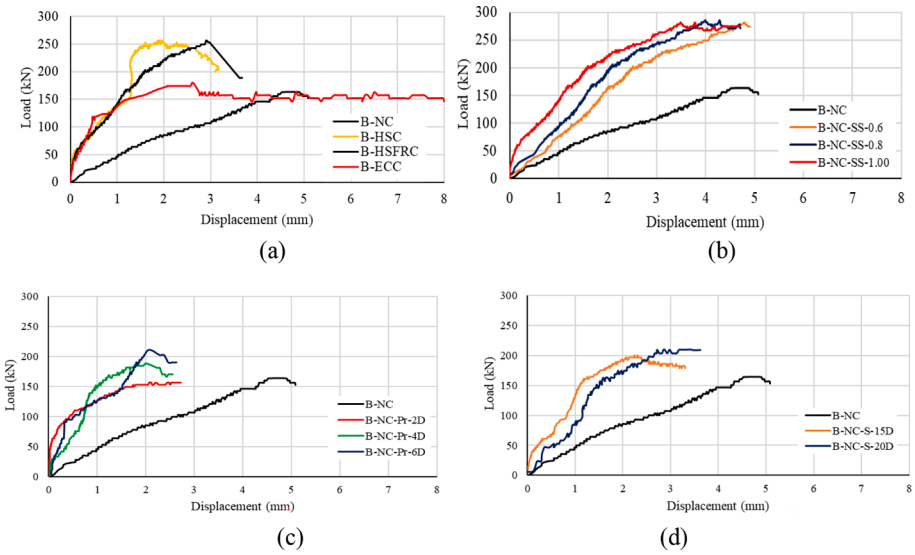

Fig. 15. Load-displacement curves: (a) Group G1, (b) Group G2, (c) Group G3, and (d) Group G4.

Table 4
Comparison between numerical and experimental results.

Specimen ID	P_{cr} (kN)			Δ_{cr} (mm)			P_u (kN)			Δ_u (mm)		
	EP	FE	FE/EX	EX	FE	FE/EX	EX	FE	FE/EX	EX	FE	FE/EX
B-NC-SS-0.6	60	62.5	1.041	0.85	0.91	1.070	279	275	0.985	4.90	4.6	0.938
B-NC-SS-0.8	70	72.1	1.031	0.71	0.74	1.042	284	295	1.038	4.28	4.4	1.028
B-NC-SS-1.0	70	73.5	1.050	0.46	0.5	1.086	283	315	1.113	3.78	4.25	1.124
Avg			1.040			1.066			1.045			1.030
SD			0.0095			0.0222			0.0643			0.0930
COV			0.913			2.082			6.15			9.029

Ex: Experimental.
FE: Finite Element Model.
Avg: Average.
SD: Standard deviation.
COV: Coefficient of variation.

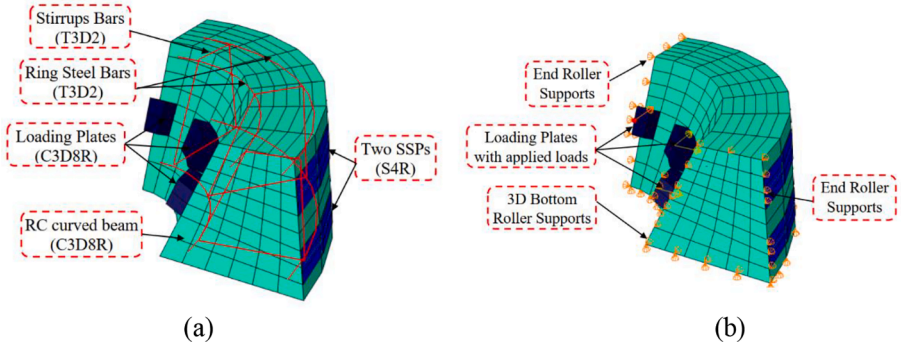

Fig. 16. Model set-up: (a) Types of all elements and meshes, and (b) Loading and boundary conditions.

test, the model was supported on roller supports. The loading and boundary conditions are shown in Fig. 16(b).

Perfect bond between the steel bars and the confined concrete was considered to simulate the interaction of concrete–steel bars. This assumption was realized by using the embedded element technique available in ABAQUS program. In this constraint, the concrete beam was the host region while the truss elements representing the reinforcement bars were selected as the embedded region as shown in Fig. 16(a). To define the constraint between the loading plates and concrete surface, full bond was assumed. The inner concrete surface of RCRBs was employed as the master while the bottom surface of the loading plates was the slave one.

4.3. Verification

The accuracy of the developed FEM is validated herein through comparing the numerical results with those obtained experimentally in terms of load–displacement response, modes of failure, and ultimate capacity. The predicted load–displacement curves of G2 specimens are compared with the experimental counterparts in Fig. 17. Both

experimental and numerical ultimate loads and their corresponding displacements are tabulated in Table 4. The main failure modes captured numerically can be seen in Fig. 17(d,e). In the same line with experimental results, all predicted load–displacement relationships have an elastic behavior up to ultimate stage.

Table 4 shows that the developed FEMs estimate very well the ultimate loads obtained experimentally since the mean values of $P_{U\ FE}/P_{U\ EXP}$ and $\Delta_{u\ FE}$ / $\Delta_{u\ EXP}$ are 1.045 and 1.03, with standard deviations of 0.064 and 0.093, respectively. In addition to the above validation against experimental results, Fig. 17 presents general failure modes detected numerically because of the excessive tensile stresses visualized at the outer side. Fig. 17(d) presents the first vertical tension crack initiated at the mid-height of the outer surface enlarging upward and downward toward the upper and lower surfaces. In this context, numerical simulation confirms that the SSPs led to the robust appearance of horizontal crack as it was observed experimentally for G2. Such cracks appeared at interface zone between the SSPs and beam surface as shown in Fig. 17(e). Fig. 18 compares the load–displacement responses predicted by the FEMs and experimental counterparts with various thicknesses. The load–displacement relationships were approximately similar for all models within initial stage and then showed similar trend of variation with gradual increase in the applied load accompanied by a larger displacement. All specimens exhibited an elastic behavior and then entered the nonlinear stage presenting hardening performance up to failure.

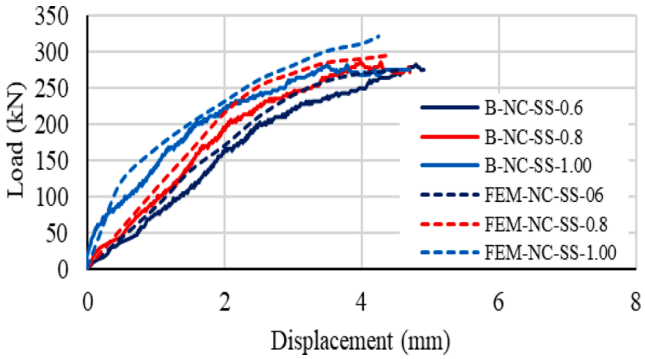

Fig. 18. Load-displacement responses of G2 specimens obtained experimentally and numerically.

5. Conclusions

This paper has reported the experiments on the behavior of twelve reinforced concrete ring beams. The effects of the concrete type, strengthening techniques, and the over lapping length of the reinforcing materials used for strengthening on the responses of such ring beams have been investigated and discussed. The nonlinear finite element models of RCRBs have been developed by means of using ABAQUS and validated by experimental data measured in this study.

Based on the experimental and numerical results of RCRBs, the following conclusions are highlighted:

- The use of HPCs could significantly increase the cracking and ultimate loads and energy absorbed capacity of RCRBs. The cracking loads (P_{cr}) of RCRBs made with HSC and HSFRC were 27% and 41% higher than that of the NC beam, respectively; the ultimate loads (P_u) were enhanced by about 54% and 57%, respectively. The use of ECC in RCRBs could improve the absorbed energy by145% compared to the beam made with NC.
- The strengthening technique using EBR with SSPs with thickness not less than about 0.60 mm could increase not only the ultimate load of the RCRB by about 70% but also its energy absorption capacity by about 60%-70%.
- The NSM strengthening technique with embedded steel bars significantly improved the elastic behavior, cracking load, and ultimate load of RCRBs. Using the NSM strengthening technique with embedded lengths of 15D and 20D increased P_{cr} by 36% and 81%, respectively; moreover, it increased the ultimate load (P_u) of the RCRB by 21% and 59%, respectively.
- The effectiveness of the prestressing strengthening technique is affected by L_o value between the two fixed end plates. It is suggested that the overlapping length should be greater than 4D. The prestressing significantly improves the elastic stiffness of RCRBs.
- The developed FE model predicted well the behavior of strengthened RCRBs with a high degree of accuracy. Therefore, the FE model can be employed to conduct parametric studies in the future.

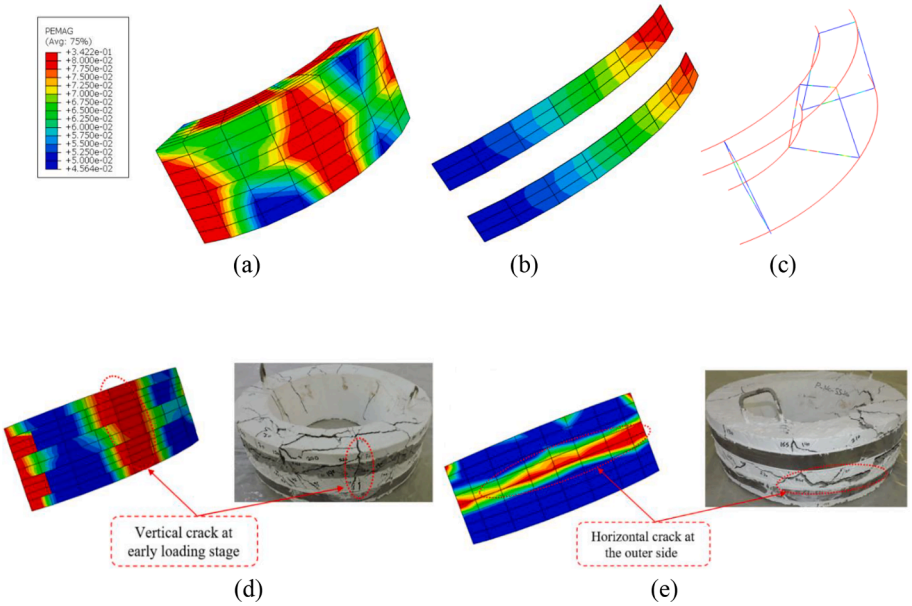

Fig. 17. FE model out-put: (a) Crack pattern observed through FEM, (b) Stress contours for SSPs, (c) Stress contours for reinforcement. (d) Vertical crack, and (e) Horizontal crack between SSPs.

CRediT authorship contribution statement

Ahmed A. Hamoda: Conceptualization, Methodology, Software, Validation, Formal analysis, Investigation, Data curation, Writing – original draft, Visualization, Project administration. **Boshra A. Eltaly:** Formal analysis, Investigation, Data curation, Writing – review & editing. **Mohamd Ghalla:** Software, Validation, Formal analysis, Investigation, Writing – review & editing. **Qing Quan Liang:** Visualization, Writing – review & editing.

Declaration of Competing Interest

The authors declare that they have no known competing financial interests or personal relationships that could have appeared to influence the work reported in this paper.

Data availability

Data will be made available on request.

References

[1] Dong B, Pan J, Cai J, Ozbakkaloglu T. Mechanical behaviour of ECC ring beam connections under square local compressive loading. J Build Eng 2021;34:101741.
[2] Peng Q, Wu H, Zhang RF, Fang Q. Numerical simulations of base-isolated LNG storage tanks subjected to large commercial aircraft crash. Thin-Walled Struct 2021;163:107660.
[3] Dilena M, Dell'Oste MF, Gubana A, Morassi A, Polentarutti F, Puntel E. Structural survey of old reinforced concrete elevated water tanks in an earthquake-prone area. Eng Struct 2021;234:111947.
[4] Pressmair N, Brosch F, Hammerl M, Kromoser B. Non-linear material modelling strategy for conventional and high-performance concrete assisted by testing. Cem Concr Res 2022;161:106933.
[5] You W, Bradford MA, Liu H, Zhao W, Yang G. Steel-alkali activated cement based ultra-high performance concrete lightweight composite bridge decks: Flexural behavior. Eng Struct 2022;266:114639.
[6] Teng L, Khayat KH. Effect of overlay thickness, fiber volume, and shrinkage mitigation on flexural behavior of thin bonded ultra-high-performance concrete overlay slab. Cem Concr Compos 2022;134:104752.
[7] Xian G, Guo R, Li C. Combined effects of sustained bending loading, water immersion and fiber hybrid mode on the mechanical properties of carbon/glass fiber reinforced polymer composite. Compos Struct 2022;281:115060.
[8] Altin S, Anil Ö, Kara ME. Improving shear capacity of existing RC beams using external bonding of steel plates. Eng Struct 2005;27:781–91.
[9] Afefy HM, Baraghith AT, Hassan A, Abuzaid MK. Strengthening of shear-deficient RC beams using near surface embedded precast cement-based composite plates (PCBCPs). Eng Struct 2021;244:112765.
[10] Zeng X, Jiang S-F, Deng K, Huang H, Cui E. Seismic performance of circular RC columns strengthened in flexure using NSM reinforcement and externally bonded BFRP sheets. Eng Struct 2022;256:114033.
[11] Bertolli V, D'Antino T. Modeling the behavior of externally bonded reinforcement using a rigid-trilinear cohesive material law. Int J Solids Struct 2022;248:111641.
[12] Siha A, Zhou C. Experimental study on hysteretic behavior of circular timber columns strengthened with wrapped CFRP strips and near surface mounted steel bars. Eng Struct 2022;263:114416.
[13] Panahi M, Zareei SA, Izadi A. Flexural strengthening of reinforced concrete beams through externally bonded FRP sheets and near surface mounted FRP bars. Case Stud Constr Mater 2021;15:e00601.
[14] Xu L-Y, Huang B-T, Qian L-P, Dai J-G. Enhancing long-term tensile performance of Engineered Cementitious Composites (ECC) using sustainable artificial geopolymer aggregates. Cem Concr Compos 2022;133:104676.
[15] Li D, Cui S, Zhang J. Experimental investigation on reinforcing effects of engineered cementitious composites (ECC) on improving progressive collapse performance of planar frame structure. Constr Build Mater 2022;347:128510.
[16] Zheng X, Gao S, Liu K, Wang F, Wu Z. Influence of zeolite internal curing on shrinkage-creep-cracking behavior of ECC and tensile property of rebar reinforced ECC. J Build Eng 2022::104669.
[17] Li N, Li WP, Lu YY, Li S. Corroded reinforced concrete columns strengthened with basalt fibre reinforced ECC under axial compression. Compos Struct 2022;116328.
[18] MohamedSalih MM, Yousif AR. Effect of reinforcement type on the behavior of rectangular HSC box-girders under combined torsion-shear-flexure: An experimental study. Structures 2022;37:536–50.
[19] Banjara NK, Ramanjaneyulu K. Experimental and numerical study on behaviour of HSFRC overlay strip strengthened flexural deficient RC beams. Eng Struct 2019;198:109561.
[20] Afefy HM, Baraghith AT, Mahmoud MH. Retrofitting of defected reinforced-concrete cantilever slabs using different techniques. Mag Concr Res 2020;72:703–19.
[21] Afefy HM, Kassem NM, Mahmoud MH. Retrofitting of faulty reinforced concrete frame structures using two strengthening techniques. Mag Concr Res 2019;71:309–24.
[22] Yang J-Q, Feng P, Liu B, Wang H, Zhao W, Hu L. Strengthening RC beams with mid-span supporting prestressed CFRP plates: An experimental investigation. Eng Struct 2022;272:115022.
[23] Zhang S, Ke Y, Chen E, Biscaia H, Li W. Effect of load distribution on the behaviour of RC beams strengthened in flexure with near-surface mounted (NSM) FRP. Compos Struct 2022;279:114782.
[24] Hamoda A, Ahmed M, Sennah K. Experimental and numerical investigations of the effectiveness of engineered cementitious composites and stainless steel plates in shear strengthening of reinforced concrete beams. Struct Concr 2022.
[25] Hamoda A, Abdelazeem F, Emara M. Concentric compressive behavior of hybrid concrete–stainless steel double-skin tubular columns incorporating high performance concretes. Thin-Walled Struct 2021;159:107297.
[26] Islam S, Young B. Effects of different adhesive and FRP on strengthening of stainless steel tubular structural members. Proceedings of the 13th International Symposium on Tubular Structures; 2010. p. 273-80.
[27] Islam SZ, Young B. Use of stainless steel as structural members in bridge construction and fiber reinforced polymer strengthening. IABSE-JSCE Joint Conference on Advances in Bridge Engineering-III, 164-173, Dhaka, Bangladesh; 2015.
[28] Joyklad P, Ali N, Chaiyasarn K, Suparp S, Hussain Q. Time-dependent behavior of full-scale precast post-tensioned (PCPT) girders: Experimental and finite element analysis. Case Stud Constr Mater 2022;17:e01310.
[29] Ma Z, Hong W. Distributed displacement estimation of pre-stressed concrete beams with random cracks using long-gauge strain sensing. Case Stud Constr Mater 2022;17:e01296.
[30] Mansouri S, Morshed R, Mostofinejad D. Using NSM pre-stressed rebars for flexural strengthening of RC beams subjected to constant loading. Structures 2022;43:1478–91.
[31] ACI Committee 318. Building code requirements for structural concrete (ACI 318-08) and commentary. American Concrete Institute; 2014.
[32] Hamoda A, Hossain K. Numerical assessment of slab–column connection additionally reinforced with steel and CFRP bars. Arab J Sci Eng 2019;44:8181–204.
[33] Carreira DJ, Chu K-H. Stress-strain relationship for plain concrete in compression. Journal Proceedings 1985;82(6):797–804.
[34] Nataraja M, Dhang N, Gupta A. Stress–strain curves for steel-fiber reinforced concrete under compression. Cem Concr Compos 1999;21:383–90.
[35] Barros JA, Figueiras JA. Flexural behavior of steel fiber reinforced concrete: testing and modelling. J Mater Civ Eng 1999;11(4):331–9.
[36] Hibbitt K, Sorensen. Inc. ABAQUS Theory Manual, User manual and ExampleManual, Version 6.7.Providence, RI. Pawtucket: Hibbitt, Karlsson & Sorensen, Inc; 2000.
[37] Lubliner J, Oliver J, Oller S, Oñate E. A plastic-damage model for concrete. Int J Solids Struct 1989;25:299–326.
[38] Ahmed M, Sheikh MN, Hadi MN, Liang QQ. Numerical modeling of self-compacting concrete columns longitudinally reinforced with steel tubes under axial loading. Eng Struct 2022;270:114913.
[39] Abrishambaf A, Barros JA, Cunha VM. Tensile stress–crack width law for steel fibre reinforced self-compacting concrete obtained from indirect (splitting) tensile tests. Cem Concr Compos 2015;57:153–65.
[40] Lee J, Fenves GL. Plastic-damage model for cyclic loading of concrete structures. J Eng Mech 1998;124:892–900.
[41] Hamoda A, Hossain K, Sennah K, Shoukry M, Mahmoud Z. Behaviour of composite high performance concrete slab on steel I-beams subjected to static hogging moment. Eng Struct 2017;140:51–65.
[42] Hamoda A, Emara M, Mansour W. Behavior of steel I-beam embedded in normal and steel fiber reinforced concrete incorporating demountable bolted connectors. Compos B Eng 2019;174:106996.
[43] Hamoda A, Basha A, Fayed S, Sennah K. Experimental and numerical assessment of reinforced concrete beams with disturbed depth. Int J Concrete Struct Mater 2019;13:1–28.
[44] Ci JC, Ahmed M, Liang QQ, Chen SC, Chen WS, Sennah K, et al. Experimental and numerical investigations into the behavior of circular concrete-filled double steel tubular slender columns. Eng Struct 2022;267:114644.
[45] Le TT, Patel VI, Liang QQ, Huynh P, Ha NS. Numerical analysis of square concrete-filled double-skin tubular columns with outer stainless-steel tube. Struct Concr 2022;23(5):2968–85.
[46] Yu K, Wang Y, Yu J, Xu S. A strain-hardening cementitious composites with the tensile capacity up to 8%. Constr Build Mater 2017;137:410–9.
[47] Yuan F, Wei W, Hu R. Shear strengthening of reinforced concrete beams with high-strength steel wire and engineered cementitious composites. Adv Struct Eng 2022;25:158–70.
[48] Feo L, Ascione F, Penna R, Lau D, Lamberti M. An experimental investigation on freezing and thawing durability of high performance fiber reinforced concrete (HPFRC). Compos Struct 2020;234:111673.
[49] Borri A, Corradi M, Castori G, Molinari A. Stainless steel strip–A proposed shear reinforcement for masonry wall panels. Constr Build Mater 2019;211:594–604.
[50] Belmouden Y, Lestuzzi P. An equivalent frame model for seismic analysis of masonry and reinforced concrete buildings. Constr Build Mater 2009;23(1):40–53.
[51] Ghahremannejad M, Abolmaali A. Prediction of shear strength of reinforced concrete beams using displacement control finite element analysis. Eng Struct 2018;169:226–37.